Suitability of eigenvalue beam-forming for discrete multi-frequency hyperthermia treatment planning

Received: 24 December 2020 | Revised: 6 August 2021 | Accepted: 6 August 2021

DOI: 10.1002/mp.15220

RESEARCH ARTICLE

MEDICAL PHYSICS

Suitability of eigenvalue beam-forming for discrete multi-frequency hyperthermia treatment planning

Massimiliano Zanoli | **Hana Dobšíček Trefná**

Department of Electrical Engineering, Chalmers University of Technology, Göteborg, Sweden

Correspondence
Massimiliano Zanoli, Department of Electrical Engineering, Chalmers University of Technology, Hörsalsvägen 11, Göteborg 41258, Sweden.
Email: zanoli@chalmers.se

Funding information
Vinnova; Barncancerfonden

Abstract

Purpose: Thermal dose delivery in microwave hyperthermia for cancer treatment is expected to benefit from the introduction of ultra-wideband (UWB)-phased array applicators. A full exploitation of the combination of different frequencies to improve the deposition pattern is, however, a nontrivial problem. It is unclear whether the cost functions used for hyperthermia treatment planning (HTP) optimization in the single-frequency setting can be meaningfully extended to the UWB case.

Method: We discuss the ability of the eigenvalue (EV) and a novel implementation of iterative-EV (i-EV) beam-forming methods to fully exploit the available frequency spectrum when a discrete set of simultaneous operating frequencies is available for treatment. We show that the quadratic power deposition ratio solved by the methods can be maximized by only one frequency in the set, therefore rendering EV inadequate for UWB treatment planning. We further investigate whether this represents a limitation in two realistic test cases, comparing the thermal distributions resulting from EV and i-EV to those obtained by optimizing for other nonlinear cost functions that allow for multi-frequency.

Results: The classical EV-based single-frequency HTP yields systematically lower target SAR deposition and temperature values than nonlinear HTP. In a larynx target, the proposed single-frequency i-EV scheme is able to compensate for this and reach temperatures comparable to those given by global nonlinear optimization. In a meninges target, the multi-frequency setting outperforms the single-frequency one, achieving better target coverage and 0.5°C higher T_{90} in the tumor than single-frequency-based HTP.

Conclusions: Classical EV performs poorly in terms of resulting target temperatures. The proposed single-frequency i-EV scheme can be a viable option depending on the patient and tumor to be treated, as long as the proper operating frequency can be selected across a UWB range. Multi-frequency HTP can bring a considerable benefit in regions typically difficult to treat such as the brain.

KEYWORDS
eigenvalue beam-forming, microwave hyperthermia, multi-frequency, treatment planning

1 | INTRODUCTION

In deep microwave hyperthermia (MW-HT) for cancer treatment, radio-frequency (RF) energy is deposited into a tumor by a phased array of antennas surrounding the patient.[1,2] The aim is to heat the tumor up to temperatures of 40–44°C, which have been proven to enhance the therapeutic effects of radio- and chemotherapy.[3,4] The challenge in deep MW-HT is to reach an adequate thermal dose coverage of the target volume while sparing the surrounding healthy tissues from excessive temperatures. To this end, each array channel is independently steered in amplitude and phase at the chosen operating frequency to shape the interference pattern

inside the patient and generate a focus in the target volume.

The list of regional deep MW-HT applicators currently used in the clinics includes systems working at 70 ∼ 100 MHz for the pelvic and abdominal region[5,6] and 434 MHz for the head and neck.[7] All these systems are designed to operate at a single frequency. The choice of this frequency is a trade-off between expected penetration depth and focal size.[8–10] The balance between these requirements might, however, change depending on the particular patient and target to be treated. If the target volume is small compared to the wavelength, a larger region is heated, which increases the risk for treatment-limiting hot-spots to arise in the adjacent healthy tissues. On the other hand, larger tumors might not be sufficiently covered by heat deposition when the focal spot is small, leaving out untreated areas. Thus, a one-fits-all operating frequency approach, while allowing for a simpler RF system design, might lead to the impossibility of achieving adequate thermal dose in some patients, resulting in their exclusion from the treatment.[11–13]

For the above reasons, an ultra-wideband (UWB) system providing the possibility to select among different operating frequencies for the treatment is desirable. The benefit is expected to be even higher if the treatment can happen at two or more concomitant and independently-steerable frequencies, as the superposition of their interference patterns might improve target coverage and hot-spot suppression.[14–16] Provided that such a system is available, the hyperthermia treatment planning (HTP) stage, where the array's steering settings are determined, has to be adapted for the UWB setting. A limited number of UWB HTP methods have been suggested in the literature: time reversal (TR) focusing,[17,18] stochastic global optimization,[10,19] quadratic programming,[15,20] and a form of eigenvalue (EV) beam-forming using finite impulse response (FIR) filters (UWB pulses).[21] The latter, FIR-based approach, would, however, require the manufacturing of an RF amplifying system with an independently programmable FIR line for each channel. This solution is difficult and costly to realize, especially with the level of accuracy required for MW-HT treatments.[22] A good compromise between robustness and complexity is given by a multi-frequency system, where two or more discrete operating frequencies are selected across the available UWB range for simultaneous or finely time-interleaved treatment.[23] TR beam-forming is a promising approach in this respect; however, current forms[24] lack the ability to properly control hot-spot formation. Recent and ongoing work is aiming at improving TR-based UWB HTP by means of iterative hot-spot suppression and cold-spot coverage.[16] Stochastic optimization, usually implemented via particle swarm (PS), is computationally demanding already in the single-frequency setting. Current applications of PS-based HTP require, in fact, a considerable coarsening of the patient model resolution to keep the execution times within reasonable limits for clinical use,[25] and research is ongoing to improve on this aspect.[26] Although PS can be easily extended to the multi-frequency problem, it is unlikely a viable option in practice due to the higher number of iterations and the longer time required for convergence when the additional amplitude and phase degrees of freedom are introduced for each new frequency.[27]

An attractive alternative for HTP optimization is the well-established EV beam-forming algorithm.[28] The problem has been thoroughly investigated in HT administered by phased arrays operating in the single-frequency setting. In particular, efforts have been spent in using EV to obtain clinically relevant solutions by defining constraints for organs at risk,[29] or by identifying regions of healthy tissue subjected to high temperatures and reoptimize the power delivered to the target with respect to those locations.[30,31] In EV-based HTP, the problem is defined as follows: find the set of steering parameters that maximizes the ratio of the average specific absorption rate (SAR) in the target to the average SAR in the healthy tissues. The problem can be solved directly because the ratio is quadratic in the unknown terms, that is, the steering parameters. This makes EV-based HTP fast and deterministic. Unfortunately, quadratic cost functions have been shown to poorly correlate with the temperature rise in the target, because they do not address the presence and severity of localized SAR peaks outside the target that can result in treatment limiting hot-spots.[32] Consequently, more suitable cost functions have been proposed to better fulfil the quality requirements of HT treatments. These cost functions are, in general, nonlinear and cannot be solved for directly via EV. Nevertheless, workarounds have been suggested in the literature to improve the EV solution with respect to such nonlinear cost functions by means of iterative procedures.[33] These procedures return good approximations of the optimal SAR deposition pattern in the single-frequency setting. Still, it is unclear whether the EV method can be meaningfully extended to the case of a discrete set of operating frequencies. Recently proposed multi-frequency constrained quadratic-programming HTP optimization methods,[15,20] while promising, do not aim at solving for the more clinically relevant nonlinear cost functions needed in HT either.

In this paper, we derive the EV problem for the multi-frequency case and show that the steering solution maximizing the SAR ratio cannot include more than one active frequency at a time. In the initial assumption that a single-frequency treatment might be sufficient, we propose a novel EV-based iterative scheme for HTP optimization that minimizes a clinically used nonlinear cost function, the *hot-spot to target quotient*[34] (HTQ). To assess the potential benefit of UWB treatments, it is necessary to understand whether the cost function (and resulting treatment plan) can be further improved by introducing additional operating frequencies. We

investigate this by developing dual-frequency treatment plans via a global stochastic optimizer (not subjected to the single-frequency limitation) and by comparing the temperature distributions resulting from single- and dual-frequency HTP optimizations in two realistic targets: one in the neck region and one in the brain.

We compare four different HTP optimization strategies, described later in Section 3. The selection of strategies is guided by the overlapping aims of the present study: (1) to assess the suitability of the average SAR ratio as objective for HTP optimization; (2) to verify the ability of the proposed fast EV-based iterative solver to reach the same HTQ optimum located by a slower global stochastic optimizer; and (3) to determine whether multi-frequency treatments can reach higher target temperatures than single-frequency ones.

2 | THEORY

In the following analysis, a lower-case a denotes a real scalar value, an upper-case A denotes a real vector value, a tilde $\tilde{a}, \tilde{A}$ denotes a complex value, and a bold symbol $\boldsymbol{a}, \boldsymbol{A}$ denotes an array or matrix. $\tilde{\boldsymbol{A}}^*$ is the element-wise complex conjugate of $\tilde{\boldsymbol{A}}$, whereas $\tilde{\boldsymbol{A}}^t$ is the transpose of $\tilde{\boldsymbol{A}}$. Field distributions and material properties are assumed to be space-dependent. In the first part of this theoretical analysis, the E-field is assumed to be linearly polarized everywhere, with local unitary direction vector denoted by $\hat{E}$. Toward the end of the analysis, the conclusions are extended to arbitrarily polarized fields by superposition.

2.1 | Eigenvalue decomposition in multi-frequency problems

Once the complex vector E-field distributions $\tilde{E}_{c,f}$ due to each channel/antenna c have been obtained inside the patient for each frequency f by means of simulations, the total field at frequency f is obtained by superposition:

$$\tilde{E}_f = \sum_c^{n_c} \tilde{p}_{c,f}\tilde{E}_{c,f} = \tilde{p}_{1,f}\tilde{E}_{1,f} + \tilde{p}_{2,f}\tilde{E}_{2,f} + \cdots + \tilde{p}_{n_c,f}\tilde{E}_{n_c,f}, \tag{1}$$

where $\tilde{p}_{c,f}$ is the steering parameter for channel c at frequency f, and n_c is the number of channels. The time-averaged power loss density $\bar{\mathcal{P}}_f$ of this sinusoidal field is given by[35]:

$$\bar{\mathcal{P}}_f = \frac{1}{2}\sigma_f||\tilde{E}_f||^2 = \frac{1}{2}\sigma_f\langle\tilde{E}_f^*, \tilde{E}_f^t\rangle = \frac{1}{2}\sigma_f\langle\tilde{\boldsymbol{p}}_f^{t*}\tilde{\boldsymbol{E}}_f^*, \tilde{\boldsymbol{E}}_f^t\tilde{\boldsymbol{p}}_f\rangle, \tag{2}$$

where σ_f is the frequency-dependent material conductivity and $\langle\cdot,\cdot\rangle$ denotes the scalar product. The quadratic vector–matrix multiplication form in the rightmost term of (2) has been obtained by expanding each $\tilde{E}_f$ with the sum in (1) and by defining the following vectors:

$$\begin{aligned}\tilde{\boldsymbol{p}}_f &= [\ \tilde{p}_{1,f}\ \tilde{p}_{2,f}\ \ldots\ \tilde{p}_{n_c,f}\ ]^t,\\ \tilde{\boldsymbol{E}}_f &= [\ \tilde{E}_{1,f}\ \tilde{E}_{2,f}\ \ldots\ \tilde{E}_{n_c,f}\ ]^t.\end{aligned} \tag{3}$$

The total SAR deposition within a volume V due to frequency f is obtained by dividing the time-averaged power $\bar{\mathcal{P}}_f$ by the material density ρ and integrating:

$$\mathrm{SAR}_f^V = \int_V \frac{\bar{\mathcal{P}}_f}{\rho}\,dv = \frac{1}{2}\tilde{\boldsymbol{p}}_f^{t*}\left(\int_V \frac{\sigma_f}{\rho}\langle\tilde{\boldsymbol{E}}_f^*, \tilde{\boldsymbol{E}}_f^t\rangle\,dv\right)\tilde{\boldsymbol{p}}_f. \tag{4}$$

The inner term within parentheses can be identified as the *SAR correlation matrix* for the volume V:

$$\tilde{\boldsymbol{q}}_f^V = \int_V \frac{\sigma_f}{\rho}\langle\tilde{\boldsymbol{E}}_f^*, \tilde{\boldsymbol{E}}_f^t\rangle\,dv \quad \in \quad \mathbb{C}^{\,n_c\times n_c}. \tag{5}$$

The single-frequency SAR focusing problem consists in determining the set of optimal steering parameters $\hat{\tilde{\boldsymbol{p}}}_f$ that maximizes the ratio of the SAR in the target volume T to the SAR in the remaining tissues R:

$$\hat{\tilde{\boldsymbol{p}}}_f = \mathrm{argmax}_{\tilde{\boldsymbol{p}}_f}\left\{\Gamma_f = \frac{\mathrm{SAR}_f^T}{\mathrm{SAR}_f^R} = \frac{\tilde{\boldsymbol{p}}_f^{t*}\tilde{\boldsymbol{q}}_f^T\tilde{\boldsymbol{p}}_f}{\tilde{\boldsymbol{p}}_f^{t*}\tilde{\boldsymbol{q}}_f^R\tilde{\boldsymbol{p}}_f}\right\}. \tag{6}$$

The ratio Γ has assumed different names in the literature, depending on which material properties are included as weighing factors in (5). Examples are the average power absorption (aPA)[9] and the SAR amplification factor (SAF)[36].

The problem (6) is a generalized eigen form[37] where the solution $\hat{\tilde{\boldsymbol{p}}}_f$ is given by the eigenvector $\boldsymbol{u}$ relative to the largest eigenvalue λ of:

$$\boldsymbol{au} = \lambda\boldsymbol{bu} \tag{7}$$

with $\boldsymbol{a} \equiv \tilde{\boldsymbol{q}}_f^T$ and $\boldsymbol{b} \equiv \tilde{\boldsymbol{q}}_f^R$. To extend the analysis to a finite set of n_f discrete frequencies, we start again from the complex E-field distribution at each frequency as given by (1). However, as the resulting field is no longer purely sinusoidal, we need to derive the time-averaged power $\bar{\mathcal{P}}$ from the real and instantaneous E, which can be described by the superposition of the fields at each frequency:

$$E = \sum_f^{n_f} E_f = \sum_f^{n_f} \hat{E}_f||\tilde{E}_f||cos(2\pi ft + \angle\langle\hat{E}_f, \tilde{E}_f\rangle). \tag{8}$$

Let us consider two separate frequencies f_i and f_j. Their resulting instantaneous power deposition in the

tissue is given by:

$$\mathcal{P} = \langle J, E\rangle = \langle \sigma_i E_i + \sigma_j E_j, E_i + E_j\rangle, \tag{9}$$

where J is the electric current density. The time-averaged power loss density is obtained by integrating $\mathcal{P}$ over a period t_0 that is common to both frequencies. Such common period might not exist if the ratio f_i/f_j is irrational. In practical cases, however, the operating frequencies can be assumed to be multiples of a base resolution (e.g., 10 MHz) and the common period can be found as the inverse of the greatest common divisor among the set: $t_0 = 1/\mathrm{GCD}(f_1, f_2, \ldots, f_{n_f})$. If the base resolution is f_0, then the common period will be at most $t_0 < 1/f_0$. For $f_0 = 10$ MHz, we have $t_0 < 100$ ns. This value has to be compared to the characteristic thermal response times of biological tissues. In particular, the periodic variations in power deposition due to the cross-frequency terms in (9) must be quicker than the conductive and perfusion cooling processes for the tissue to experience negligible fluctuations in temperature during treatment. This is indeed the case, as the typical time constants for thermal washout in HT lie in the order of minutes.[38] Thus, it is safe to assume that the resulting power distribution can always be time-averaged for HTP evaluation purposes. The time-averaged power deposition can be obtained as:

$$\bar{\mathcal{P}} = \frac{1}{t_0}\int_{-t_0/2}^{+t_0/2} \mathcal{P}\, dt = \frac{1}{t_0}\int_{-t_0/2}^{+t_0/2} \langle \sigma_i E_i + \sigma_j E_j, E_i + E_j\rangle\, dt. \tag{10}$$

The scalar product in (10) can be expanded using (8). The cross-frequency terms $\cos(2\pi f_i)\cdot\cos(2\pi f_j)$ resulting from this multiplication have zero mean over the common period t_0. The only terms thus left are $\cos^2(2\pi f_i)$ and $\cos^2(2\pi f_j)$, yielding:

$$\bar{\mathcal{P}} = \frac{1}{2}\sigma_i ||\tilde{E}_i||^2 + \frac{1}{2}\sigma_j ||\tilde{E}_j||^2, \tag{11}$$

which is the sum of the independent contributions from each frequency, in the same form as (2). This result is valid for an arbitrary number n_f of separate discrete operating frequencies, and generalizes as follows:

$$\bar{\mathcal{P}} = \sum_f^{n_f} \frac{1}{2}\sigma_f ||\tilde{E}_f||^2 = \sum_f^{n_f} \frac{1}{2}\sigma_f \langle \tilde{\boldsymbol{p}}_f^{t*}\tilde{\boldsymbol{E}}_f^{*}, \tilde{\boldsymbol{E}}_f^{t}\tilde{\boldsymbol{p}}_f\rangle. \tag{12}$$

To preserve the compact quadratic vector–matrix multiplication form, the steering parameter vectors and the power correlation matrices can be concatenated into:

$$\tilde{\boldsymbol{p}} = \left[\tilde{\boldsymbol{p}}_1^t\ \tilde{\boldsymbol{p}}_2^t \ldots \tilde{\boldsymbol{p}}_{n_f}^t\right]^t, \tag{13}$$

$$\tilde{\boldsymbol{q}}^V = \begin{bmatrix} \tilde{\boldsymbol{q}}_1^V & 0 & \cdots & 0 \\ 0 & \tilde{\boldsymbol{q}}_2^V & \cdots & 0 \\ \vdots & \vdots & \ddots & \vdots \\ 0 & 0 & \cdots & \tilde{\boldsymbol{q}}_{n_f}^V \end{bmatrix} \in \mathbb{C}^{(n_c n_f)\times(n_c n_f)}, \tag{14}$$

where $\tilde{\boldsymbol{q}}^V$ is block diagonal. The overall SAR deposition within a volume V resulting from the sum in (12) can then be expressed as:

$$\mathrm{SAR}^V = \tilde{\boldsymbol{p}}^{t*}\tilde{\boldsymbol{q}}^V\tilde{\boldsymbol{p}}, \tag{15}$$

and the SAR focusing problem (6) is generalized to many frequencies as:

$$\hat{\tilde{\boldsymbol{p}}} = \mathrm{argmax}_{\tilde{\boldsymbol{p}}}\left\{\Gamma = \frac{\mathrm{SAR}^T}{\mathrm{SAR}^R} = \frac{\tilde{\boldsymbol{p}}^{t*}\tilde{\boldsymbol{q}}^T\tilde{\boldsymbol{p}}}{\tilde{\boldsymbol{p}}^{t*}\tilde{\boldsymbol{q}}^R\tilde{\boldsymbol{p}}}\right\}. \tag{16}$$

An important consequence of $\tilde{\boldsymbol{q}}^V$ being block diagonal is that the eigenvectors and eigenvalues of (16) are all and only those of the individual $\tilde{\boldsymbol{q}}_f^V$ blocks.[39] This means that only an eigenvector of the following form can maximize Γ:

$$\hat{\tilde{\boldsymbol{p}}} = [\,\boldsymbol{0}\ \ldots\ \hat{\tilde{\boldsymbol{p}}}_f^t\ \ldots\ \boldsymbol{0}\,]^t, \tag{17}$$

where only one operating frequency f is active, and that there is no combination of two or more frequencies that can further improve this ratio. In other words, the optimal target-to-remaining average SAR ratio can be achieved only with one frequency, even if a discrete set of separate operating frequencies is available. Thus, maximizing Γ as objective function in HTP optimizations via (16) will always result in treatment plans consisting of only one operating frequency, regardless of how many discrete frequencies have been included in the optimization problem.

This result might at first seem in contradiction with Zastrow et al,[21] where the weights of a FIR filter are jointly optimized to maximize the SAR ratio. However, that study adopts a continuous wideband approach, leading to different conclusions than those drawn in the present case. In particular, FIR filters are described by continuous and smooth frequency spectra,[40] such that $\tilde{p}(f) \approx \tilde{p}(f + df)$ for any frequency f and small increment df. This implies strong correlation between nearby frequencies, so that the time-averaged power $\bar{\mathcal{P}}$ is no longer given by (12).

In the last part of this theoretical analysis, we extend the conclusions to arbitrarily polarized fields. When the applicator feeds are designed for single polarization, as is generally the case in MW-HT, a second polarization might still appear locally in the treated domain due to the complex geometrical scattering affecting the wave

propagation in the patient. If the main polarization component of the E-field at frequency f is denoted with $\tilde{E}_f^{\parallel}$ and the orthogonal polarization component with $\tilde{E}_f^{\perp}$, such that $\tilde{E}_f = \tilde{E}_f^{\parallel} + \tilde{E}_f^{\perp}$ and $\langle \tilde{E}_f^{\parallel}, \tilde{E}_f^{\perp} \rangle = 0$, the time-averaged power deposition (2) becomes:

$$\bar{\mathcal{P}}_f = \frac{1}{2}\sigma_f ||\tilde{E}_f||^2 = \sigma_f \frac{1}{2}\left(||\tilde{E}_f^{\parallel}||^2 + ||\tilde{E}_f^{\perp}||^2 \right) \tag{18}$$

in view of the orthogonality between the two components. As the second polarization stems from the same feed excitation, it is subject to the same amplitude and phase steering of the main polarization. Therefore, the power deposition can be expressed as a function of the steering parameters as:

$$\begin{aligned} \bar{\mathcal{P}}_f &= \frac{1}{2}\sigma_f \langle (\tilde{E}_f^{\parallel} + \tilde{E}_f^{\perp})^*, (\tilde{E}_f^{\parallel} + \tilde{E}_f^{\perp})^t \rangle = \frac{1}{2}\sigma_f \langle \tilde{\boldsymbol{p}}_f^{t*} (\tilde{\boldsymbol{E}}_f^{\parallel} + \tilde{\boldsymbol{E}}_f^{\perp})^*, (\tilde{\boldsymbol{E}}_f^{\parallel} + \tilde{\boldsymbol{E}}_f^{\perp})^t \tilde{\boldsymbol{p}}_f \rangle \\ &= \frac{1}{2}\sigma_f \langle \tilde{\boldsymbol{p}}_f^{t*} \tilde{\boldsymbol{E}}_f^*, \tilde{\boldsymbol{E}}_f^t \tilde{\boldsymbol{p}}_f \rangle, \end{aligned} \tag{19}$$

which is the same form as (2).

2.2 | Iterating EV to solve for a nonlinear HTP cost-function

As SAR^V represents an average of all the SAR values in volume V, no considerations are made over the actual distribution of SAR within the volume. In other words, using the plain integral in (5) might result in unacceptably high SAR peaks in the healthy tissues (hot-spots) or insufficient coverage of certain tumor areas. To improve on this aspect, a weighing distribution $w(v)$ can be introduced.[31,33] The SAR matrix calculation (5) becomes:

$$\tilde{\boldsymbol{q}}_f^V = \int_V w \frac{\sigma_f}{\rho} \langle \tilde{\boldsymbol{E}}_f^*, \tilde{\boldsymbol{E}}_f^t \rangle \, dv. \tag{20}$$

In general, the weight distribution cannot be determined beforehand, but the EV procedure can be iterated by updating w according to the resulting SAR distribution. Starting with an initial weight distribution $w_0(v) = 1, \ \forall \, v$, we propose the following update scheme to determine the next set of weights w_{n+1} from iteration n:

$$w_{n+1}(v) = \begin{cases} w_n(v) + 1 & v \in R1 \\ w_n(v) & v \notin R1, \end{cases} \tag{21}$$

where $R1$ is the subset of remaining healthy tissues containing the highest 1-percentile of SAR. Note that the $R1$ set is not necessarily connected, and it can include several hot-spots across the volume of healthy tissues. An iteration can be considered successful if it improved the SAR deposition within the target and reduced the peak hot-spot(s) in healthy tissues, represented by $R1$. To this end, the *hot-spot to target quotient*[34] (HTQ) can be used:

$$\mathrm{HTQ} = \frac{\overline{\mathrm{SAR}}_{R1}}{\overline{\mathrm{SAR}}_T}, \tag{22}$$

where $\overline{\mathrm{SAR}}_T$ is the average SAR in the target, and $\overline{\mathrm{SAR}}_{R1}$ is the average SAR in the most prominent hot-spot(s). This HTP quality indicator can be used as a nonlinear cost function for the iterative process, which consists in applying (21) until the HTQ no longer improves. At each iteration, the SAR peaks in the healthy tissues are given more importance in the computation of the Γ ratio, which results in the driving vector $\hat{\boldsymbol{p}}$ progressively steering the power deposition away from those locations. Because of the target SAR term in the denominator of (22) and the limited aperture of the applicator array, the overall power deposition is not reduced but rather redirected toward other healthy regions with less exposure. Eventually, this power redistribution process reaches a plateau where further modifications cannot reduce the main SAR peak without also increasing the secondary lobe above it, at which point the HTQ deteriorates and the procedure is halted. The overall single-frequency iterative EV (i-EV) procedure is explained in detail with a flowchart in Figure 1 and compared to other single- and multi-frequency optimization strategies for HTP throughout the rest of this article.

3 | MATERIALS AND METHODS

To benchmark the proposed iterative scheme, highlight the limits of single-frequency HTP, and investigate the overall suitability of the SAR ratio as cost function for HTP, we consider two examples of realistic targets treated with single- and multi-frequency MW-HT. The first target is anatomically identified in the larynx, whereas the second is a meningioma (Figure 2). The applicator arrays consist of 10 wideband self-grounded bow-tie antennas[41] each (Figure 3), working across the 400–800 MHz frequency band. The applicators include a surface and an antenna water bolus that fulfil three purposes: cool the patient's skin, realize a dielectric matching between antenna and patient, and reduce cross-coupling between nearby antennas. The set of operating frequencies available for treatment is obtained by stepping 100 MHz within the antenna operational frequency band for the single-frequency case and considering all possible two-frequency combinations for the multi-frequency case, yielding a total of 15 operating frequency settings.

The upper body part used in electromagnetic and thermal simulations is a subset of the *Duke* human voxel model from the IT'IS Foundation,[42] and all healthy tissue properties are obtained from the IT'IS Database.[43]

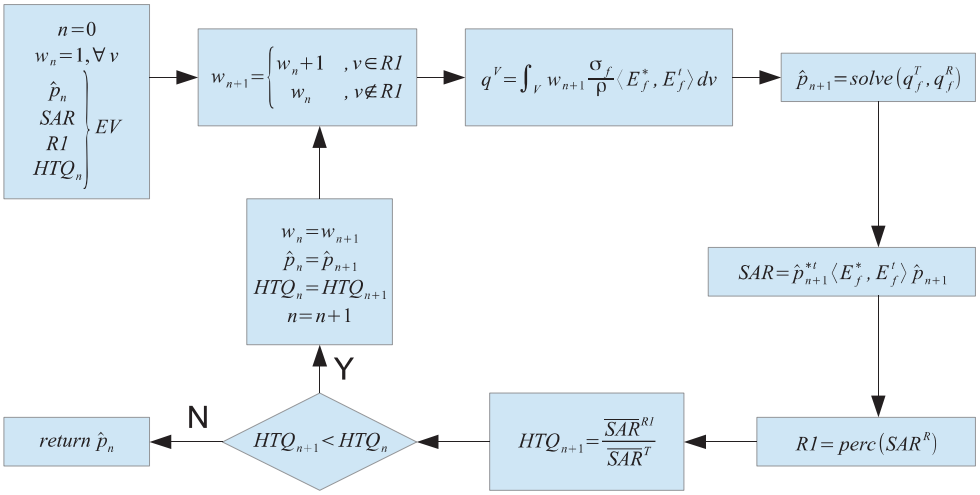

FIGURE 1 Flowchart of the proposed eigenvalue (EV)-based iterative scheme for single-frequency HTP (i-EV), whose aim is to minimize the HTQ. The procedure is initiated at the EV solution that maximizes the Γ ratio with uniform weighing. The *R*1 subset is determined by the `perc()` function as the 1% of remaining healthy tissues with the highest SAR values. The `solve()` function determines the optimal set of steering parameters using EV to solve (6)

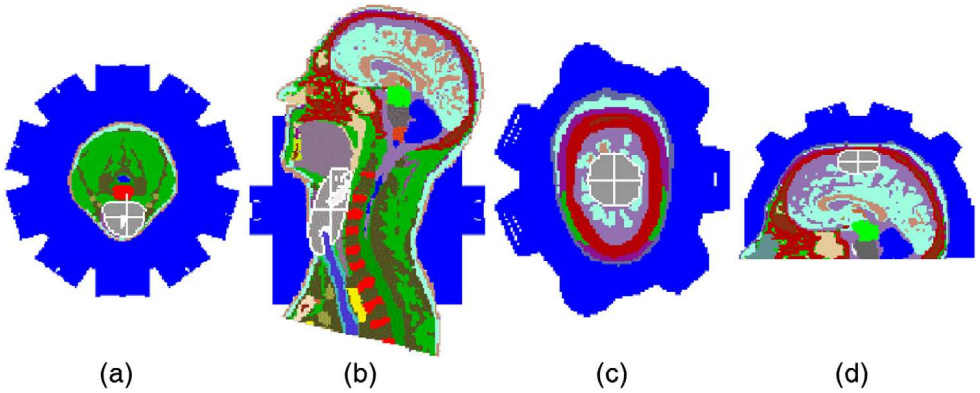

FIGURE 2 Patient models: (a) transverse and (b) sagittal sections of the neck setup, (c) transverse, and (d) sagittal sections of the brain setup. The targets are outlined in white. The target center is indicated by a white cross. The blue shades represent the water bolus

The E-field and temperature distributions, generated by a circular array for the neck and a semispherical array for the brain, are obtained via the commercial solver CST Microwave Studio®.[44] For HTP optimization and quality assessment purposes, the SAR distributions are smoothed by a 1 g mass averaging scheme. Surface voxels are treated by expanding the convolution kernel until the mass of tissue within reaches 1 g.

For the electromagnetic simulations, we utilize the standard finite-difference time-domain (FDTD) technique implemented in the solver. The domain is meshed into a hexahedral grid with resolution varying from 0.4 mm at the antennas (metal sheet thickness) to 10 mm in the air surrounding the patient, for a total of 125 million cells for the larynx model and 219 million cells for the meningioma model. The antenna feeds are excited by discrete ports. Biological tissues and water are modeled as dispersive materials. Absorbing boundary conditions are enforced at all domain boundaries. For the thermal simulations, we choose the available

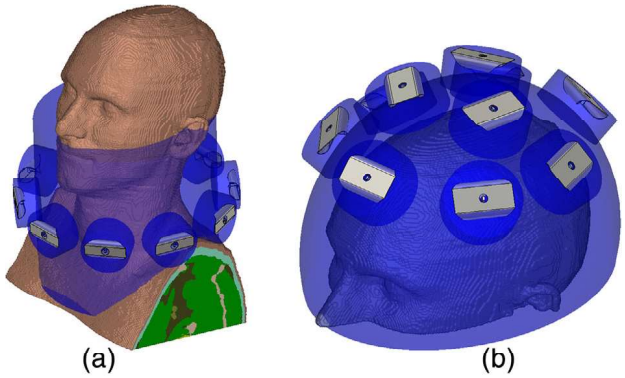

FIGURE 3 Applicator models: (a) neck applicator for the larynx target and (b) brain applicator for the meningioma target. The blue shades represent the water bolus

TABLE 1 Properties of the tumor materials used to fill the target volumes. Relative permittivity (ε_r), electric conductivity (σ), density (ρ), thermal conductivity (k), heat capacity (c), perfusion coefficient (ω_b), and metabolic heat (Q_m)

Tumor	ε_r [~]	σ [$\frac{S}{m}$]	ρ [$\frac{kg}{m^3}$]	k [$\frac{W}{K\,m}$]	c [$\frac{kJ}{K\,kg}$]	ω_b [$\frac{kW}{K\,m^3}$]	Q_m [$\frac{kW}{m^3}$]
Larynx	47.8	0.674	1088	0.423	3.285	22.033	5.456
Meninges	57.3	1.372	1063	0.535	3.754	17.048	5.478

steady-state solver. The mesh is hexahedral with fixed 1 mm resolution. The water bolus temperature is set to 30°C for the larynx patient and 20°C for the meningioma patient. Only conductive heat transport is modeled at the skin–air interface. Open boundaries are adopted for the thermal simulations as well.

The tumor targets (Figure 2) are manually delineated inside the model and filled with a material exhibiting dielectric and thermal properties equal to the weighted average of the materials originally composing the volume. Some thermal properties are further adjusted to reflect the response of tissues to thermal stress: muscle perfusion is increased by a factor 4 due to the systemic response to heat,[45] tumor perfusion is decreased by a factor 0.7 to account for its chaotic vasculature,[46] and the thermal conductivity of the cerebrospinal fluid is increased by a factor 10 to emulate the convective transport of heat.[47] The resulting tumor properties are reported in Table 1.

We compare the SAR distributions obtained via different HTP methods using two clinically established quality indicators: the HTQ, as defined above in (22), and the 50% *iso-SAR target coverage* (TC_{50}) defined as follows[48,49]:

$$TC_{50} = \frac{|T'|}{|T|} \quad , \quad T' \mid \mathrm{SAR}[T'] \geq \frac{1}{2}\mathrm{SAR}[R \cup T], \quad (23)$$

where SAR[V] is any SAR value in volume V, and T' is a subset of the target volume. In words, this value represents the fraction of target volume whose SAR values are above 50% of the highest SAR peak in the patient. We further assess the thermal distributions obtained when either Γ, HTQ, or TC_{50} are used as cost functions for the SAR-based HTP. In thermal simulations, the power deposition is scaled until the temperature peak in healthy tissues reaches 43°C.[50–52] The quality of each distribution is then evaluated in terms of target median temperature, T_{50}, and temperature reached by 90% of the target volume, T_{90}. The four investigated HTP methods are labeled as follows:

`EV[Γ]`	solving for the Γ ratio via EV
`i-EV[HTQ]`	minimizing the HTQ via iterative EV
`PS[HTQ]`	minimizing the HTQ via PS
`PS[TC_50]`	maximizing the TC_{50} via PS

where PS stands for particle swarm, a global stochastic optimizer capable of solving single- and multi-frequency problems for nonlinear cost functions.[53] All HTP algorithms are implemented in MATLAB®[54] and run on a high-performance GPU (nVidia® Quadro™ RTX6000).

4 | RESULTS

Figure 4 reports the optimal values of the SAR absorption ratio Γ for each individual frequency for both targets. These values are obtained by directly solving (6) using EV decomposition. The power ratio exhibits a clear frequency-dependent behavior, with one frequency yielding the highest Γ value. The values achieved by other frequencies decrease nearly monotonically with the distance from this optimal frequency. In terms of raw power ratio, the ideal frequency for the larynx target is 800 MHz, whereas for the meningioma, it is 400 MHz.

To show the convergent properties and highlight the computational performances of the proposed i-EV optimization method, we report in Figure 5 the cost function value as a function of the cost function evaluations performed by the algorithm in an exemplary HTP case and compare it with the evaluations needed by PS to converge to the same optimum. The global stochastic optimizer needs 5000 cost function evaluations to reach an HTQ value of 0.82, whereas the iterative-weighed EV decomposition i-EV only needs around 50 evaluations to reach a comparable HTQ value of 0.85. In terms of GPU computational times, PS takes 126 s, whereas i-EV takes only 6 s. Similar optimal values and orders of magnitude in speed improvement are observed for all the single-frequency HTP problems considered in this study.

The assessment of each HTP in terms of HTQ is reported in Figure 6 and Table 2. The benefit introduced by shifting from a single- to a multi-frequency setting is indicated by the gray bars in the plots. Naturally, the methods that aim at minimizing the HTQ, such as `i-EV[HTQ]` and `PS[HTQ]`, yield the lowest (i.e., best) values for this indicator. Noticeably, i-EV is capable of minimizing the HTQ to levels comparable to the global optimum provided by PS in all single-frequency cases. At 600 MHz, in the larynx case, the HTQ provided by i-EV is even lower than PS's, indicating that PS might not have converged to the global optimum. The SAR distributions resulting from direct EV, which solves for the maximum Γ, exhibit consistently high HTQ (> 1.18), regardless of the frequency. Similarly, high HTQ values are obtained even by the PS optimization when TC_{50} is used as a goal function. Inspection of eventual enhancements in

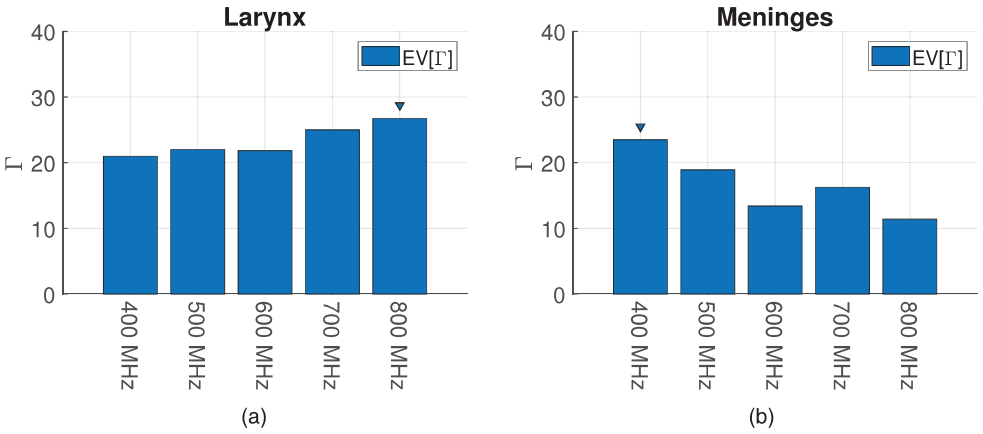

FIGURE 4 The maximum SAR absorption ratio, Γ, at each single operating frequency for the two selected targets, obtained via direct solution. The triangle indicates the best Γ value and operating frequency for a given model

TABLE 2 HTQ values of the HTPs obtained via the specified optimization methods for the two selected targets and for all frequency combinations. EV and i-EV can only handle single-frequency plans. Best values for method and frequency setting are reported in bold and underlined. Best overall values per patient model are highlighted in gray

HTQ	Larynx				Meninges			
***f* [MHz]**	EV[Γ]	i-EV[HTQ]	PS[HTQ]	PS[TC_50]	EV[Γ]	i-EV[HTQ]	PS[HTQ]	PS[TC_50]
400	**1.18**	0.87	0.83	**1.16**	1.54	1.26	1.21	1.71
500	1.25	**0.85**	**0.82**	1.20	**1.38**	**1.24**	1.16	**1.25**
600	1.21	0.90	0.97	1.28	1.41	1.24	**1.15**	1.42
700	1.19	0.95	0.94	1.22	1.38	1.25	1.16	1.62
800	1.22	1.03	1.01	1.35	1.46	1.32	1.20	1.71
400 + 500			0.83	1.22			1.13	1.37
400 + 600			0.82	1.17			1.11	1.44
400 + 700			0.82	1.22			1.16	1.35
400 + 800			0.82	1.24			1.15	1.51
500 + 600			0.82	1.24			1.14	1.44
500 + 700			0.82	1.22			**1.07**	**1.33**
500 + 800			**0.82**	**1.17**			1.08	1.35
600 + 700			0.90	1.32			1.07	1.34
600 + 800			0.93	1.31			1.11	1.39
700 + 800			0.94	1.35			1.11	1.39

the multi-frequency setting reveals that, in terms of HTQ, virtually, no improvement is achieved in either target.

Figure 7 and Table 3 report the values of TC_{50} as quality indicator for each HTP. The difference in TC_{50} between the best single- and multi-frequency solutions reveals that the benefit of introducing a second operating frequency is negligible in the larynx case (from 84% @ 400 MHz to 86% @ 400 + 700 MHz), but relevant in the meningioma case (from 63% @ 500 MHz to 73% @ 400 + 700 MHz). The PS[TC_50] solution at 600 + 700 MHz gains more than 10% in TC_{50} for the meningioma target with respect to the best single-frequency solution. The HTQ-optimal solutions, i-EV[HTQ] and PS[HTQ], yield poor target coverage in almost all cases. In particular, TC_{50} in the meninges is extremely low for these solutions (< 30%). At 500 MHz, PS[HTQ] gains about 16% in target coverage with respect to i-EV[HTQ], despite the negligible difference of 0.07 in HTQ between the two solutions seen in Figure 6(b). In the larynx, only one single-frequency case and two multi-frequency cases yield coverage above 50% when solved for HTQ. The EV[Γ] solutions yield poor target coverage in all cases. The PS[TC_50] optimization strategy yields the best values for this indicator, as expected.

To gain a better understanding of the differences between the HTP methods considered in this work, the

TABLE 3 TC_{50} values (%) of the HTPs obtained via the specified optimization methods for the two selected targets and for all frequency combinations. EV and i-EV can only handle single-frequency plans. Best values for method and frequency setting are reported in bold and underlined. Best overall values per patient model are highlighted in gray

TC_{50}	Larynx				Meninges			
***f* [MHz]**	EV[Γ]	i-EV[HTQ]	PS[HTQ]	PS[TC_50]	EV[Γ]	i-EV[HTQ]	PS[HTQ]	PS[TC_50]
400	**26.8**	**57.6**	**60.1**	**84.0**	9.4	**13.4**	13.8	37.6
500	22.7	38.8	33.1	80.9	8.7	13.2	**28.8**	**62.9**
600	24.6	43.4	45.5	70.0	11.1	10.7	11.5	55.6
700	24.1	22.9	22.4	64.7	8.4	10.5	12.6	38.9
800	17.1	25.3	24.0	48.8	**12.9**	12.9	12.7	32.9
400 + 500			45.4	84.2			**21.3**	67.8
400 + 600			44.7	84.6			12.2	56.7
400 + 700			51.4	**85.5**			16.8	65.3
400 + 800			**53.1**	84.5			14.2	57.0
500 + 600			32.2	85.1			14.3	61.6
500 + 700			32.7	84.4			20.7	71.0
500 + 800			29.1	83.5			19.1	66.2
600 + 700			37.8	76.6			14.3	**73.2**
600 + 800			35.4	71.4			13.3	66.6
700 + 800			23.0	69.4			14.4	63.8

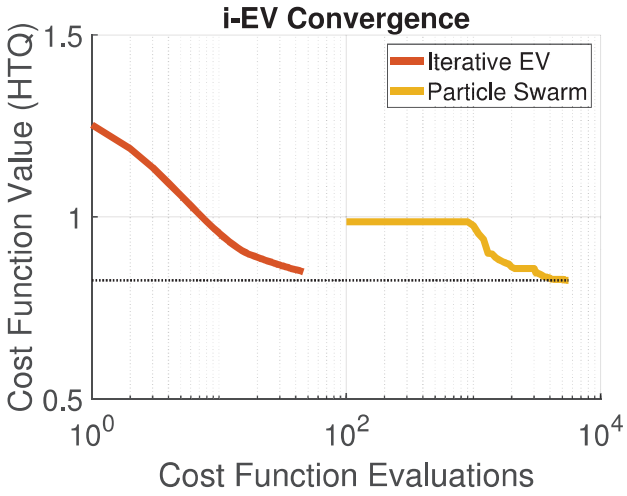

FIGURE 5 Example of convergence for the i-EV and PS algorithms in a single-frequency treatment planning optimization problem using HTQ as cost function. Larynx target, 500 MHz. The black dotted line indicates the optimum determined by PS. i-EV starts at the classic EV solution and determines a solution very close to the optimal one after only about 50 evaluations. PS needs 100 evaluations to complete its first iteration only, and the optimum is reached after more than 5000 evaluations

SAR distributions achieved by each method at its optimal combination of frequencies in terms of final cost function value are visualized in Figures 8 and 9. In the larynx case, the EV[Γ] solution at 800 MHz reflects the poor target coverage, especially in deeper parts of the target, and the inefficient hot-spot suppression suggested by the values of the HTP quality indicators. The main heating spot is outside the target and located in the adjacent skin layer between the target and the bolus. The i-EV[HTQ] and PS[HTQ] solutions exhibit very similar SAR patterns, with relatively homogeneous energy deposition thorough the target and maxima located near the target center. This correspondence can be explained by the major contribution of the frequency component at 500 MHz. The role of the second frequency component at 800 MHz in the PS[HTQ] solution is rather limited; nevertheless, it increases the SAR deposition in the deeper parts of the tumor by radiation from the antennas lying on the posterior side of the neck. The PS[TC_50] optimization strategy yields a remarkably different solution from all the previous methods. In this solution, almost all antennas are active and their power contribution is in the same order of magnitude. This results in a very high and homogeneous energy deposition in the tumor, which is, however, accompanied by considerable heating of the surrounding healthy tissues. In fact, both superficial and deep healthy tissue heating spots are present in this solution.

In the meningioma case, Figure 9, the main SAR peak of the EV[Γ] solution is located inside the target. Nevertheless, this peak is rather narrow and only affects the superficial part of the tumor, leaving the deeper parts unheated. The i-EV[HTQ] slightly improves on this aspect by extending the SAR deposition into the deeper parts of the brain. The PS[HTQ] method further enhances the coverage of deeper tumor areas with the help of a second frequency component at 700 MHz. The PS[TC_50] solution once more distinguishes itself from the other methods by actively using all antennas and frequency components to considerably extend the

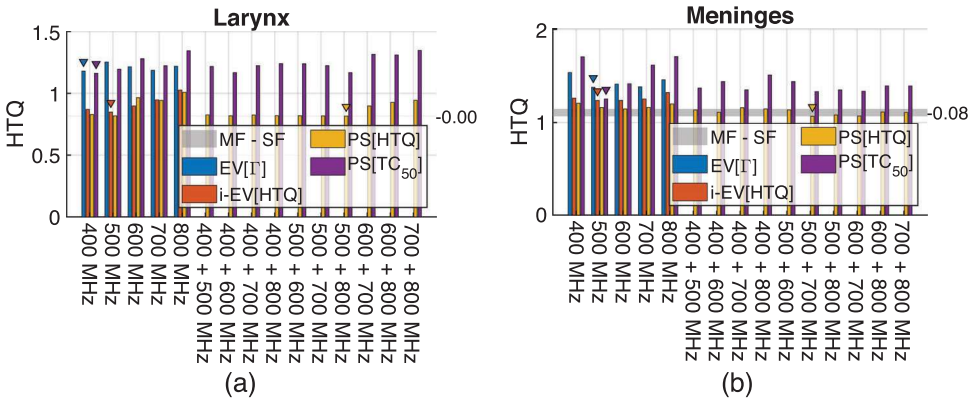

FIGURE 6 HTQ values for the two selected targets and for all frequency combinations, obtained via the methods specified in the legend. The triangles indicate the best result and frequency combination for the corresponding method. The gray `MF - SF` bar and the value next to it report the difference between the best single-frequency result and the best multi-frequency result

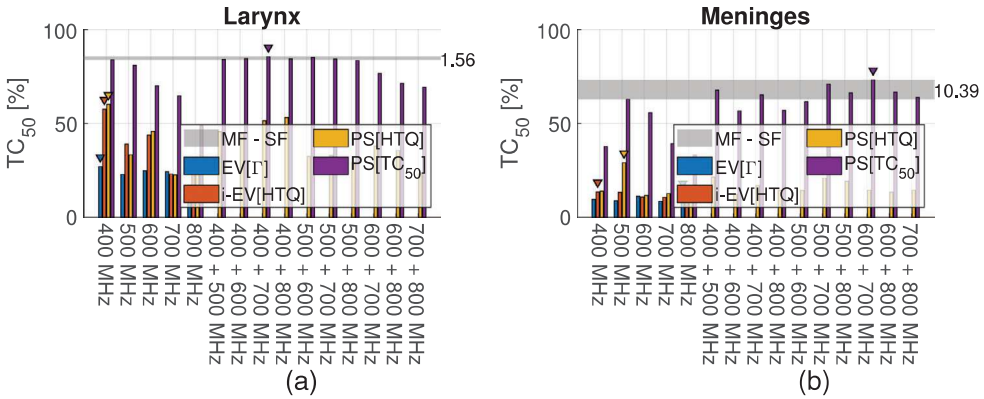

FIGURE 7 TC_{50} for the two selected targets and for all frequency combinations, obtained via the methods specified in the legend. The triangles indicate the best result and frequency combination for the corresponding method. The gray `MF - SF` bar and the value next to it report the difference between the best single-frequency result and the best multi-frequency result

SAR deposition throughout the whole target volume. This is done at the expenses of a substantial heating of the healthy tissues; however, the heating spots are now located more superficially and closer to the water bolus than in the larynx case.

Figures 10 and 11 report the temperature profiles obtained from the above-mentioned plans after thermal simulations. Again, each profile corresponds to the frequency combination that yielded the best cost function value for the given optimization algorithm. The analysis of the temperature distributions obtained inside the targets is summarized into cumulative histograms in Figure 12, whereas the median temperature T_{50} and 90-percentile temperature T_{90} achieved in the target volumes are reported in Table 4.

For the larynx case, the `EV[Γ]` solution results in high temperatures in the frontal area of the target ($\approx 44°C$), whereas the deeper parts of the target, behind the trachea, do not achieve therapeutic temperatures ($\approx 38°C$), as expected from the low SAR values at this location. The resulting median and 90-percentile target temperatures are therefore relatively low, below 40°C and 39°C, respectively. The `i-EV[HTQ]` and `PS[HTQ]` methods yield similar distributions, with most of the target volume reaching 40°C in both cases. The performances of the single-frequency `i-EV[HTQ]` and `PS[HTQ]` are almost identical, as predicted by their similar HTQ and TC_{50} values and SAR distributions. In the TC_{50}-optimal solution, the main temperature peak is found outside the target (43°C, as per constraint), near the spinal cord. This results in a median target temperature 0.8°C lower than the HTQ-optimal solutions. However, the temperature homogeneity inside the target is still high, achieving the same value of T_{90} as for `i-EV[HTQ]` and `PS[HTQ]`.

In the meninges, the `EV[Γ]` solution results in neither a localized high temperature peak nor good coverage. The cooling effect of the water bolus counteracts the high SAR deposition close to the skull, damping the temperature peak (42.8°C). The cumulative histogram indicates that most of the tumor is subjected to

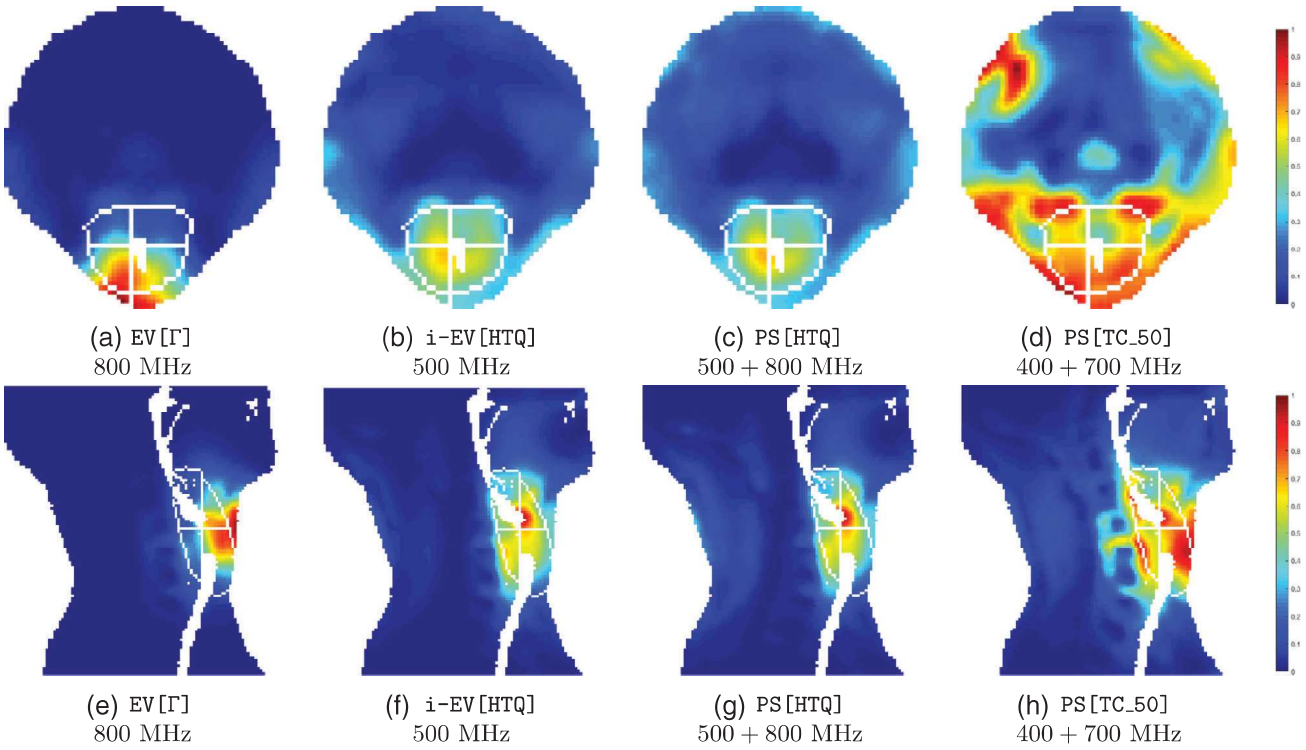

FIGURE 8 SAR distributions in the larynx case for each optimization strategy at its optimal frequency or combination of frequencies. (a)–(d) transverse sections and (e)–(h) sagittal sections. The target is outlined in white. The sections are taken at the target center, which is indicated by a white cross. The SAR values are normalized to the highest peak inside the patient. The SAR is not calculated for those voxels belonging to background or to the patient's lumina, because they do not represent biological tissue

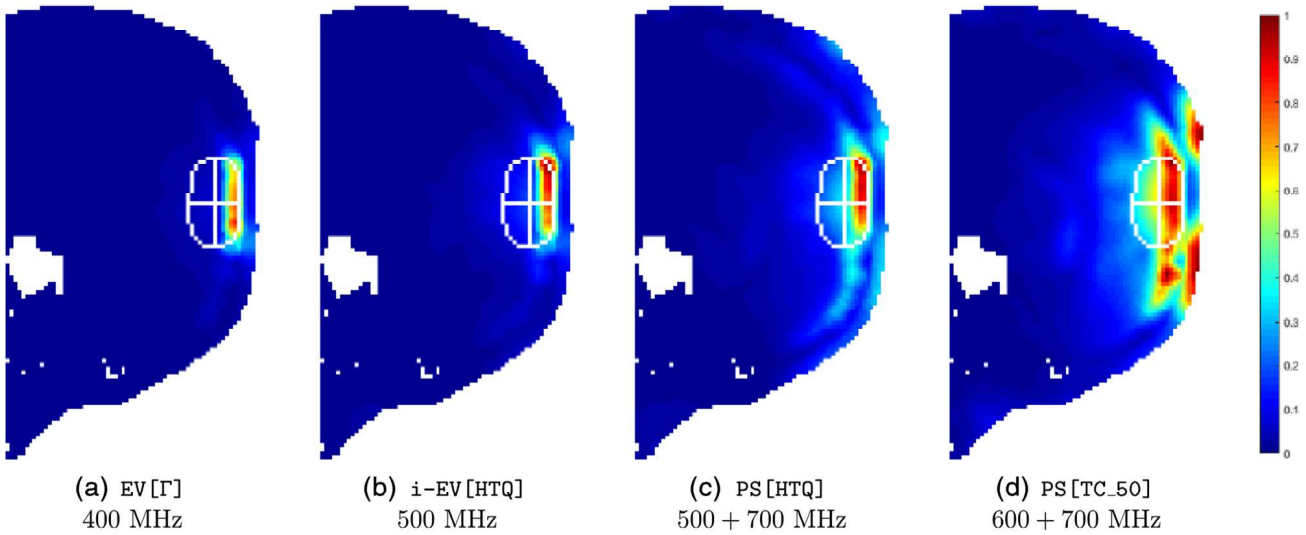

FIGURE 9 SAR distributions in the meninges case for each optimization strategy at its optimal frequency or combination of frequencies. Sagittal sections. The target is outlined in white. The sections are taken at the target center, which is indicated by a white cross. The SAR values are normalized to the highest peak inside the patient. The SAR is not calculated for those voxels belonging to background or to the patient's lumina, because they do not represent biological tissue. The sections are rotated by 90° for optimal layout

temperatures below 40°C. The single-frequency i-EV[HTQ] solution partially improves on this aspect by shifting the power deposition toward the deeper part of the target. The most relevant enhancement of the median and 90-percentile temperatures is, however, achieved by the multi-frequency solutions PS[HTQ] and PS[TC_50]. The PS[HTQ] solution utilizing two frequencies gains 1.2°C both in T_{50} and T_{90} with respect to

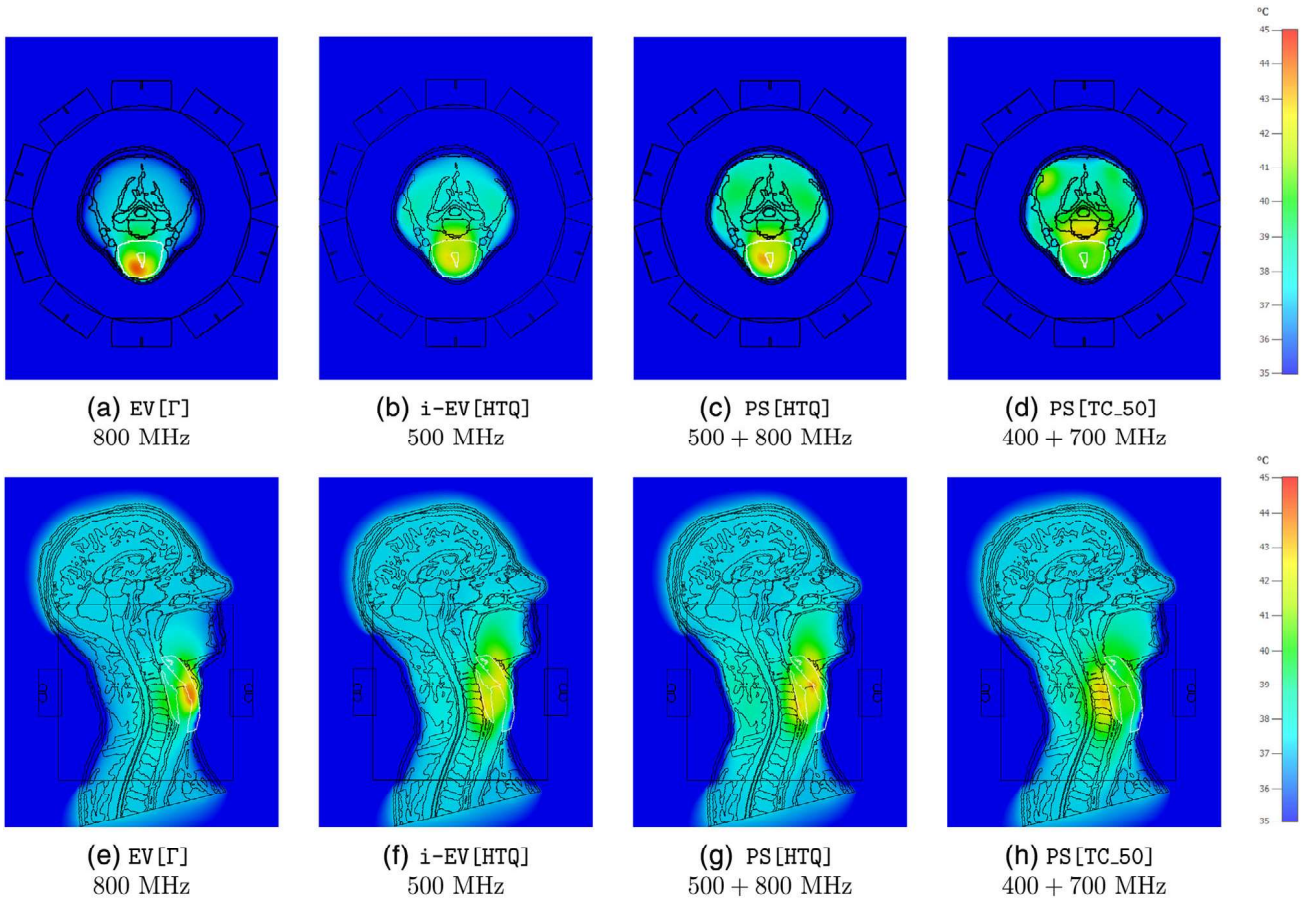

FIGURE 10 Temperature distributions achieved in the larynx case by the SAR-based treatment plans at their optimal frequency or combination of frequencies. (a)–(d) Transverse sections and (e)–(h) sagittal sections. The target is outlined in white. The maximum temperature in the healthy tissues is 43°C in all cases

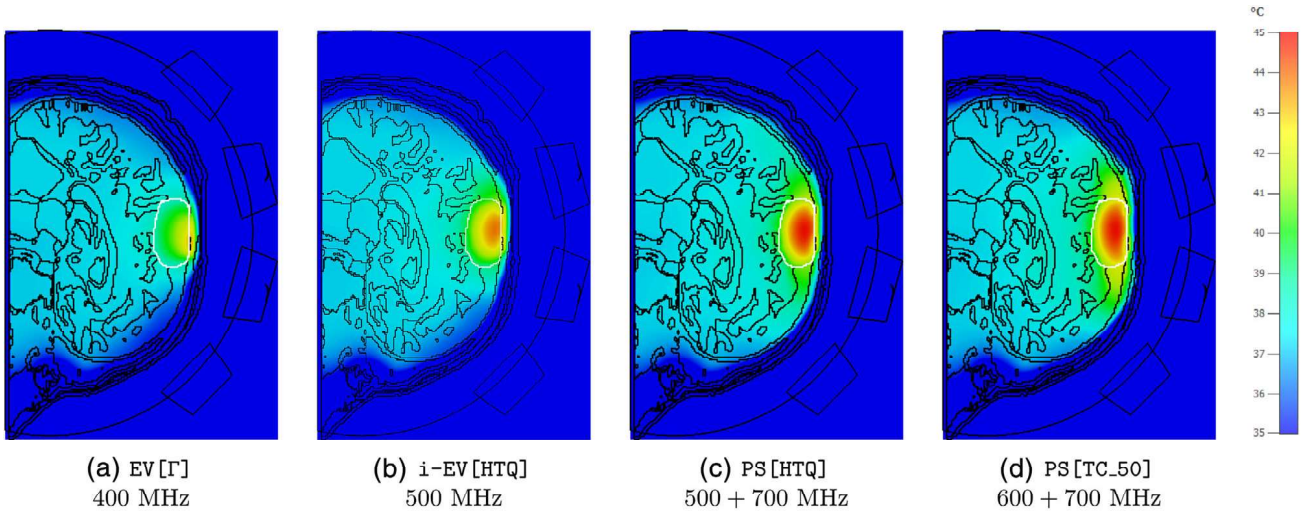

FIGURE 11 Temperature distributions achieved in the meninges case by the SAR-based treatment plans at their optimal frequency or combination of frequencies. Sagittal sections. The target is outlined in white. The maximum temperature in the healthy tissues is 43°C in all cases. The sections are rotated by 90° for optimal layout

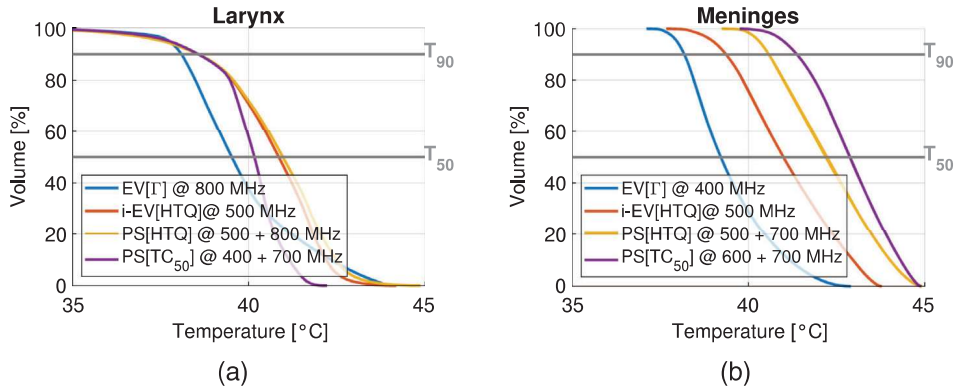

FIGURE 12 Cumulative histograms of the temperatures reached inside the two selected targets. The gray lines indicate the reference for the 50th and 90th volume percentiles

TABLE 4 Median and 90-percentile temperature values in the targets, for each HTP method at its optimal frequency combination (***f***)

	Larynx				Meninges			
	`EV[Γ]`	`i-EV[HTQ]`	`PS[HTQ]`	`PS[TC_50]`	`EV[Γ]`	`i-EV[HTQ]`	`PS[HTQ]`	`PS[TC_50]`
f [MHz]	800	500	500 + 800	400 + 700	400	500	500 + 700	600 + 700
T_{50} [°C]	39.5	40.9	41.0	40.2	39.2	41.0	42.2	42.9
T_{90} [°C]	38.1	38.6	38.6	38.6	38.2	39.4	40.6	41.4

the single-frequency `i-EV[HTQ]`. The multi-frequency TC_{50}-optimal solution further increases both temperature indicators, gaining 0.7°C in T_{50} and 0.8°C in T_{90} with respect to `PS[HTQ]`.

To further investigate the benefits of including a second operating frequency in the meningioma example, we report the cumulative histograms of the temperatures inside the target for the TC_{50}-optimal solutions in the single-frequency and multi-frequency cases in Figure 13. In the multi-frequency setting, the cumulative curve is steeper and above the single-frequency one, indicating that high temperatures are achieved across the entire target volume. The addition of a second frequency improves notably the T_{50} and T_{90} values by about 0.3 and 0.5°C, respectively.

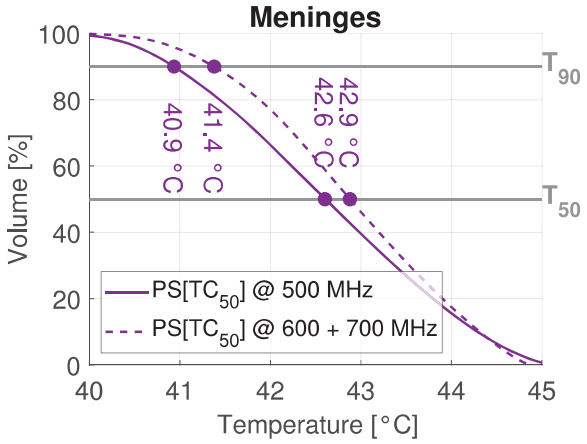

FIGURE 13 Cumulative histograms of the temperatures reached inside the meningioma target using the TC_{50}-best single-frequency (solid line) and multi-frequency (dashed line) solutions. The gray lines indicate the reference for the 50th and 90th volume percentiles. The dots further report the actual values of T_{50} and T_{90} for these solutions

5 | DISCUSSION

The present work discusses the capability of several SAR-based HTP optimization strategies to shape the SAR pattern inside the patient and focus the heating in the target, while at the same time limiting the power deposition peaks and thus potential hot-spots in the healthy tissues. The investigation includes single- and multiple-frequency schemes. In particular, it is designed to address several and partly overlapping objectives: (1) to assess the suitability of Γ as objective for HTP optimization (`EV[Γ]` vs. nonlinear cost-function-based optimizers `i-EV` and `PS`); (2) to verify the ability of the proposed fast EV-based iterative solver for HTQ to reach the same optimum located by a slower global stochastic optimizer (`i-EV[HTQ]` vs. `PS[HTQ]`); (3) to determine whether multi-frequency treatments can reach higher target temperatures than single-frequency ones (`EV`, `i-EV` and single-frequency `PS` versus multi-frequency `PS`). The choice of PS as counterpart for the assessment of EV is motivated by the fact that both solvers are actively used in clinical practice.[19,55]

The outcome of HT treatments has been shown to correlate with the temperatures achieved in the treated region. A strong evidence for this comes from the

successful clinical trials,[12,56–58] but also from the studies that failed to demonstrate the benefit of HT due to poor heating quality.[59,60] Various thermal dose metrics have been proposed to exploit this correlation, and their relationship with the therapeutic effect has been validated in retrospective clinical studies. The methods investigated in this study are evaluated using clinically relevant metrics. In particular, the 25% iso-SAR contour (TC_{25}) has been suggested as a predictive SAR-based factor for clinical outcome.[48] More recently, Bellizzi et al[49] suggested TC_{50} to correlate better with the achieved temperatures in more challenging locations such as the head and neck. According to clinical practice, tumor coverage is evaluated by the indexed temperatures T_{10}, T_{50}, and T_{90}, which represent the temperatures achieved in at least 10%, 50%, and 90% of the target volume, respectively.

As a consequence of uncertainties in thermal modeling, the current clinical practice still relies on increasing the applied power until the temperature in the most critical hot-spot reaches the maximum allowed temperature or causes discomfort to the patient. The constraints of 43–45°C to healthy tissues in the treatment planning reflect the general acceptance among the clinicians.[52] In our evaluation, we take a conservative approach and scale the input power such that healthy tissue temperatures do not exceed 43°C. In this way, the comparison between the different HTP strategies reflects the expected clinical gain.

5.1 | Suitability of Γ as objective for HTP optimization

Maximizing the quadratic ratio (6) between the average power deposition in the target and the average power deposition in the remaining healthy tissues is a classic way to achieve EM focusing in a subregion of a domain. This problem can be efficiently solved using EV decomposition, as shown in Section 2. In fact, EV beam-forming for HTP was introduced almost three decades ago[28] and is still repeatedly used in the clinical setting albeit with modifications and improvements.[31,33] Still to date, the power ratio (6) and EV-based HTP are considered a means to evaluate the heating capabilities of an applicator design prior its clinical use.[36,61]

The clinical implementation of HTP in the past decade, however, revealed that the average power deposition is not a good predictor of the thermal distribution achieved inside the treated region, and that local hot-spots in healthy tissues are more relevant limiting factors.[62,63] The temperature profiles relative to the Γ-optimal solutions reported in Figure 12 and Table 4 confirm this limitation. The median target temperature achieved by the $\mathrm{EV}[\Gamma]$ plan is about 1.5 and 3.7°C lower than the best solutions in the larynx and the meninges, respectively. More modern HTP cost functions, such as the HTQ, overcome the limitation of the average operator. Unfortunately, their intrinsic nonlinearity hinders a direct solution and requires an iterative procedure such as the i-EV proposed here or similar strategies.[33] At the same time, the use of fast direct-iterative solvers instead of slower global stochastic optimizers such as PS is still desirable, due to the high speed required for online HTP adjustments in the clinical setting.[64]

5.2 | Using a fast eigenvalue-based iterative solver (i-EV)

The SAR-based analysis carried out in this work indicates that the proposed i-EV scheme based on (21) is capable of reaching HTQ values that are comparable to those yielded by a global stochastic optimizer for different operating frequencies and array topologies. This is, however, valid only when the treatment options are limited to a single operating frequency. In particular, the larynx case suggests that a single-frequency treatment might be sufficient for this patient, as long as the most suitable frequency can be selected across a UWB range. Note, in fact, that both HTQ and TC_{50} exhibit frequency-dependent behaviors regardless of the optimization algorithm used (Figures 6 and 7, Tables 2 and 3).

The results further indicate that the suitability of the chosen HTP cost function is also region- and target-dependent. The HTQ-optimal temperature distribution performs better than the TC_{50}-optimal one in terms of median and peak temperatures in the larynx case. In the meningioma case, however, the situation is reversed and the TC_{50}-based HTP appears to be the best choice. This might be due to a number of factors. First of all, the presence of the skull in close contact with the cerebrospinal fluid generates sharp and narrow SAR peaks that might be better captured by the local peak term used in the TC_{50} definition. In contrast, HTQ considers the hot-spot as a larger subvolume of healthy tissues (1%), which might be too coarse to accurately identify the location of the limiting peak. Note that defining the hot-spot as 1% of the patient model also renders the HTQ values model-dependent, thus preventing meaningful direct comparisons between the two cases. Efforts to combine the two distinct treatment objectives of target coverage and hot-spot suppression in a single volume-independent optimization metric are ongoing.[65]

5.3 | The potential of multi-frequency HTP to increase the thermal dose in the target

The thermal distributions achieved in the mengioma case indicate that MW-HT treatments can benefit considerably from the multi-frequency approach in this region. In the best case, using TC_{50} as cost function,

the multi-frequency approach yields $T_{50} = 42.9°C$ and $T_{90} = 41.4°C$ versus $T_{50} = 42.6°C$ and $T_{90} = 40.9°C$ for the best single-frequency solution, implying that the temperatures are higher and more uniformly distributed across the target volume. The use of a second frequency is particularly beneficial in increasing the tumor coverage, demonstrated by a 0.5°C gain in T_{90}. The advantages of the multi-frequency setting are also highlighted when considering the HTQ as a cost function for HTP. The single-frequency `i-EV[HTQ]` results in 1.2°C lower T_{50} than the multi-frequency `PS[HTQ]`.

The assessment of the clinical potential of the multi-frequency approach must be done from the point of view of the thermal dose relationship predicting the cytotoxic effect of HT treatments. Clinical protocols require high T_{10}, T_{50}, and T_{90} temperatures to be maintained for a specified amount of time.[56] T_{90}, in particular, has been shown to correlate with clinical outcome.[66,67] To incorporate the notions of temperature and treatment duration into one metric, the *cumulative equivalent minutes at* $T_{90} = 43°C$ ($CEM_{43}T_{90}$) metric has been proposed and its dose-effect relationship has been reported.[11] A strong relationship between the achieved tumor temperature and the cytotoxic effect, as modeled by the $CEM_{43}T_{90}$ metric, suggests that a decrease of 1°C from the reference temperature of 43°C inside the tumor corresponds to a fourfold decrease in the resulting thermal dose, underlining the importance of striving for higher tumor temperatures.

In view of remaining uncertainties affecting patient modeling, the reliability of thermal simulations in HTP must be discussed. In fact, the recent report by Aklan et al[68] uncovered that the *absolute* temperature values predicted by thermal simulations still do not correlate sufficiently well with measured temperatures during treatment. In that study, differences between predicted and measured temperatures reached up to 2°C on average. Nevertheless, *relative* changes in temperature following amplitude and phase steering have been shown to correlate extremely well between simulations and actual treatments,[69] with predictions as accurate as 0.1°C. In this report, we compare relative changes in thermal distributions, and therefore, expect the simulated improvements to reflect in the clinical scenario. As such, an increase of half a degree in T_{90} achieved by the multi-frequency plan in the meningioma case would correspond to a doubling of the thermal dose for the same treatment duration, according to the $CEM_{43}T_{90}$ model (for $T_{90} < 43°C$). This higher dose, in turn, is expected to reflect into better tumor response.[12] Although the expected benefit is lower for $T_{90} > 43°C$, such high values for T_{90} are rarely achieved in clinical practice,[12] due to the known challenges in external heating. This further stresses the paramount importance of struggling for higher and more homogeneous temperatures, and the present investigation indicates that multi-frequency can be one way to reach this goal.

As a final note, we acknowledge that the potential and suitability of the multi-frequency approach needs to be assessed over a larger patient data set.

6 | CONCLUSION

This study discusses the suitability of classic EV beamforming for HTP, proposes a novel iterative scheme that improves the single-frequency EV-based HTP, and investigates the potential advantages of multi-frequency versus single-frequency HTP. As previously found in other studies, the examples reported here indicate that EV in its basic form should be avoided as HTP method, because it yields target temperatures far below the desired therapeutic values. However, EV can still be used in its iterative form to minimize nonlinear cost functions for single-frequency HTP problems, when one frequency is sufficient to achieve target coverage and hot-spot suppression. The operational frequency should nevertheless be carefully selected from a wide frequency band depending on the tumor size and location. In fact, as this study highlights, the quality indicators in single-frequency plans exhibit a strong dependence on the selected operating frequency. Consequently, a modern applicator should be designed to allow for the selection of the operating frequency across a ultra-wide range. In regions such as the brain, the use of two or more concomitant frequencies can considerably improve the thermal distributions, increasing median temperature and temperature homogeneity within the target while not exceeding the set temperature limit in healthy tissues. Overall, these results suggest that a comparison between applicators and plans should not be grounded on average power ratios, but rather on nonlinear indicators such as HTQ and TC_{50}, and further motivate the design and development of UWB applicators for MW-HT.

ACKNOWLEDGMENT

This work was financially supported by the VINN EXcellence Center of ChaseOn (Chalmers Antenna Systems) and The Swedish Childhood Cancer Fund.

CONFLICT OF INTEREST

The authors report no conflict of interest.

DATA AVAILABILITY STATEMENT

Data sharing is not applicable to this article as no new data sets were generated during the current study.

REFERENCES

1. Stauffer PR, Paulides MM. Hyperthermia therapy for cancer. *Compr Biomed Phys*. 2014;10:115-151.
2. Paulides MM, Trefna HD, Curto S, Rodrigues DB. Recent technological advancements in radiofrequency-and microwave-mediated hyperthermia for enhancing drug delivery. *Adv Drug Deliv Rev*. 2020;163-164:3-18.

3. Datta NR, Rogers S, Ordóñez SG, Puric E, Bodis S. Hyperthermia and radiotherapy in the management of head and neck cancers: a systematic review and meta-analysis. *Int J Hyperthermia*. 2016;32:31-40.
4. Elming PB, Sørensen BS, Oei AL, et al.. Hyperthermia: the optimal treatment to overcome radiation resistant hypoxia. *Cancers*. 2019;11:60.
5. Crezee J, Van Haaren PMA, Westendorp H, et al.. Improving locoregional hyperthermia delivery using the 3-D controlled AMC-8 phased array hyperthermia system: a preclinical study. *Int J Hyperthermia*. 2009;25:581-592.
6. Zweije R, Kok HP, Bakker A, Bel A, Crezee J. Technical and clinical evaluation of the ALBA-4D 70MHz loco-regional hyperthermia system. In: *2018 48th European Microwave Conference (EuMC)*. IEEE; 2018:328-331.
7. Paulides MM, Rijnen Z, Togni P, et al. Clinical introduction of novel microwave hyperthermia technology: the HYPERcollar3D applicator for head and neck hyperthermia. In: *2015 9th European Conference on Antennas and Propagation (EuCAP)*. IEEE; 2015:1-4.
8. Seebass M, Beck R, Gellermann J, Nadobny J, Wust P. Electromagnetic phased arrays for regional hyperthermia: optimal frequency and antenna arrangement. *Int J Hyperthermia*. 2001;17:321-336.
9. Paulides MM, Vossen SHJA, Zwamborn APM, Rhoon GC. Theoretical investigation into the feasibility to deposit RF energy centrally in the head-and-neck region. *Int J Radiat Oncol Biol Phys*. 2005;63:634-642.
10. Kok HP, De GM, Borsboom PP, Bel A, Crezee J. Improved power steering with double and triple ring waveguide systems: the impact of the operating frequency. *Int J Hyperthermia*. 2011;27:224-239.
11. Jones EL, Oleson JR, Prosnitz LR, et al.. Randomized trial of hyperthermia and radiation for superficial tumors. *J Clin Oncol*. 2005;23:3079-3085.
12. Franckena M, Fatehi D, Bruijne M, et al.. Hyperthermia dose-effect relationship in 420 patients with cervical cancer treated with combined radiotherapy and hyperthermia. *Eur J Cancer*. 2009;45:1969-1978.
13. Paulides MM, Verduijn GM, Van Holthe N. Status quo and directions in deep head and neck hyperthermia. *Radiat Oncol*. 2016;11:1-14.
14. Converse M, Bond EJ, Veen BD, Hagness C. A computational study of ultra-wideband versus narrowband microwave hyperthermia for breast cancer treatment. *IEEE Trans Microwave Theory Technol*. 2006;54:2169-2180.
15. Kuehne A, Oberacker E, Waiczies H, Niendorf T. Solving the time- and frequency-multiplexed problem of constrained radiofrequency induced hyperthermia. *Cancers*. 2020;12:1072.
16. Zanoli M, Trefna HD. Iterative time-reversal for multi-frequency hyperthermia. *Phys Med Biol*. 2020;66:045027.
17. Guo B, Xu L, Li J. Time reversal based microwave hyperthermia treatment of breast cancer. *Microwave Opt Technol Lett*. 2005;47:335-338.
18. Trefná HD, Vrba J, Persson M. Time-reversal focusing in microwave hyperthermia for deep-seated tumors. *Phys Med Biol*. 2010;55:2167.
19. Paulides MM, Stauffer PR, Neufeld E, et al.. Simulation techniques in hyperthermia treatment planning. *Int J Hyperthermia*. 2013;29:346-357.
20. Bellizzi GG, Crocco L, Battaglia GM, Isernia T. Multi-frequency constrained SAR focusing for patient specific hyperthermia treatment. *IEEE J Electromagnet RF Microw Med Biol*. 2017;1:74-80.
21. Zastrow E, Hagness SC, Van Veen BD. 3D computational study of non-invasive patient-specific microwave hyperthermia treatment of breast cancer. *Phys Med Biol*. 2010;55:3611.
22. Bruggmoser G, Bauchowitz S, Canters R, et al.. Quality assurance for clinical studies in regional deep hyperthermia. *Strahlenther Onkol*. 2011;187:605.
23. Trefná HD, Martinsson B, Petersson T, et al. Multifrequency approach in hyperthermia treatment planning: impact of frequency on SAR distribution in head and neck. In: *2017 11th European Conference on Antennas and Propagation (EUCAP)*. IEEE; 2017:3710-3712.
24. Takook P, Dobsicek TH, Zeng X, Fhager A, Persson M. A computational study using time reversal focusing for hyperthermia treatment planning. *Prog Electromagn Res*. 2017;73:117-130.
25. Rijnen Z, Bakker JF, Canters RAM, et al.. Clinical integration of software tool VEDO for adaptive and quantitative application of phased array hyperthermia in the head and neck. *Int J Hyperthermia*. 2013;29:181-193.
26. Cappiello G, Mc Ginley B, Elahi MA, et al.. Differential evolution optimization of the SAR distribution for head and neck hyperthermia. *IEEE Trans Biomed Eng*. 2016;64:1875-1885.
27. Pedersen MEH. *Good Parameters for Particle Swarm Optimization*. Technical Report HL1001, Hvass Lab., Copenhagen, Denmark; 2010:1551-3203.
28. Böhm M, Kremer J, Louis AK. Efficient algorithm for computing optimal control of antennas in hyperthermia. *Surveys Math Indust*. 1993;3:233-251.
29. Bardati F, Borrani A, Gerardino A, Lovisolo GA. SAR optimization in a phased array radiofrequency hyperthermia system. *IEEE Trans Biomed Eng*. 1995;42:1201-1207.
30. Das SK, Clegg ST, Samulski TV. Computational techniques for fast hyperthermia temperature optimization. *Med Phys*. 1999;26:319-328.
31. Köhler T, Maass P, Wust P, Seebass M. A fast algorithm to find optimal controls of multiantenna applicators in regional hyperthermia. *Phys Med Biol*. 2001;46:2503.
32. Canters RAM, Wust P, Bakker JF, Van Rhoon GC. A literature survey on indicators for characterisation and optimisation of SAR distributions in deep hyperthermia, a plea for standardisation. *Int J Hyperthermia*. 2009;25:593-608.
33. Mestrom RMC, Van Engelen JP, Van Beurden MC, Paulides MM, Numan WCM, Tijhuis AG. A refined eigenvalue-based optimization technique for hyperthermia treatment planning. In: *The 8th European Conference on Antennas and Propagation (EuCAP 2014)*. IEEE; 2014:2010-2013.
34. Canters RAM, Franckena M, Paulides MM, Van Rhoon GC. Patient positioning in deep hyperthermia: influences of inaccuracies, signal correction possibilities and optimization potential. *Phys Med Biol*. 2009;54:3923.
35. Cheng DK. *Field and Wave Electromagnetics*. Addison-Wesley Series in Electrical Engineering. Addison-Wesley Publishing Company; 1989.
36. Guérin B, Villena JF, Polimeridis AG, et al.. Computation of ultimate SAR amplification factors for radiofrequency hyperthermia in non-uniform body models: impact of frequency and tumour location. *Int J Hyperthermia*. 2018;34:87-100.
37. Ghojogh B, Karray F, Crowley M. Eigenvalue and generalized eigenvalue problems: tutorial. *arXiv preprint arXiv:1903.11240*. 2019.
38. Samulski TV, Fessenden P, Valdagni R, Kapp DS. Correlations of thermal washout rate, steady state temperatures, and tissue type in deep seated recurrent or metastatic tumors. *Int J Radiat Oncol Biol Phys*. 1987;13:907-916.
39. Dasgupta B. *Applied Mathematical Methods*. Always Learning. Dorling Kindersley; 2006.
40. Mohanty NC. *Signal Processing: Signals, Filtering, and Detection*. Springer; 2012.
41. Takook P, Persson M, Gellermann J, Trefná HD. Compact self-grounded Bow-Tie antenna design for an UWB phased-array hyperthermia applicator. *Int J Hyperthermia*. 2017;33:387-400.

42. Gosselin M-C, Neufeld E, Moser H, et al.. Development of a new generation of high-resolution anatomical models for medical device evaluation: the Virtual Population 3.0. *Phys Med Biol*. 2014;59:5287.
43. Hasgall PA, Di Gennaro F, Baumgartner C, et al. IT'IS Database for thermal and electromagnetic parameters of biological tissues. 2018.
44. Dassault Systèmes SE, Vélizy-Villacoublay F. CST Studio Suite 2019. 2019.
45. Rossmann C, Haemmerich D. Review of temperature dependence of thermal properties, dielectric properties, and perfusion of biological tissues at hyperthermic and ablation temperatures. *Crit Rev Biomed Eng*. 2014;42:467-492.
46. Lang J, Erdmann B, Seebass M. Impact of nonlinear heat transfer on temperature control in regional hyperthermia. *IEEE Trans Biomed Eng*. 1999;46:1129-1138.
47. Schooneveldt G, Trefná HD, Persson M, et al.. Hyperthermia treatment planning including convective flow in cerebrospinal fluid for brain tumour hyperthermia treatment using a novel dedicated paediatric brain applicator. *Cancers*. 2019;11:1183.
48. Lee HK, Antell AG, Perez CA, et al.. Superficial hyperthermia and irradiation for recurrent breast carcinoma of the chest wall: prognostic factors in 196 tumors. *Int J Radiat Oncol Biol Phys*. 1998;40:365-375.
49. Bellizzi GG, Drizdal T, Rhoon GC, Crocco L, Isernia T, Paulides MM. Predictive value of SAR based quality indicators for head and neck hyperthermia treatment quality. *Int J Hyperthermia*. 2019;36:455-464.
50. Sapareto SA, Dewey WC. Thermal dose determination in cancer therapy. *Int J Radiat Oncol Biol Phys*. 1984;10:787-800.
51. Yarmolenko PS, Moon EJ, Landon C, et al.. Thresholds for thermal damage to normal tissues: an update. *Int J Hyperthermia*. 2011;27:320-343.
52. Trefná HD, Crezee H, Schmidt M, et al.. Quality assurance guidelines for superficial hyperthermia clinical trials: I. Clinical requirements. *Int J Hyperthermia*. 2017;33:471-482.
53. Clerc M. *Particle Swarm Optimization*. John Wiley & Sons; 2010:93.
54. The MathWorks Inc., Natick, Massachusetts. MATLAB R2019 2019.
55. Kok HP, Kotte ANTJ, Crezee J. Planning, optimisation and evaluation of hyperthermia treatments. *Int J Hyperthermia*. 2017;33:593-607.
56. Sherar M, Liu F-F, Pintilie M, et al.. Relationship between thermal dose and outcome in thermoradiotherapy treatments for superficial recurrences of breast cancer: data from a phase III trial. *Int J Radiat Oncol Biol Phys*. 1997;39:371-380.
57. Wessalowski R, Schneider DT, Mils O, et al.. Regional deep hyperthermia for salvage treatment of children and adolescents with refractory or recurrent non-testicular malignant germ-cell tumours: an open-label, non-randomised, single-institution, phase 2 study. *Lancet Oncol*. 2013;14:843-852.
58. Issels RD, Lindner LH, Verweij J, et al.. Effect of neoadjuvant chemotherapy plus regional hyperthermia on long-term outcomes among patients with localized high-risk soft tissue sarcoma: the EORTC 62961-ESHO 95 randomized clinical trial. *JAMA Oncol*. 2018;4:483-492.
59. Perez CA, Gillespie B, Pajak T, Hornback NB, Emami D, Rubin P. Quality assurance problems in clinical hyperthermia and their impact on therapeutic outcome: a report by the Radiation Therapy Oncology Group. *Int J Radiat Oncol Biol Phys*. 1989;16:551-558.
60. Perez CA, Pajak T, Emami B, Hornback NB, Tupchong L, Rubin P. Randomized phase III study comparing irradiation and hyperthermia with irradiation alone in superficial measurable tumors. Final report by the Radiation Therapy Oncology Group. *Am J Clin Oncol*. 1991;14:133-141.
61. Bardati F, Tognolatti P. Hyperthermia phased arrays pretreatment evaluation. *Int J Hyperthermia*. 2016;32:911-922.
62. Canters RAM, Franckena M, Zee J, Van Rhoon GC. Optimizing deep hyperthermia treatments: are locations of patient pain complaints correlated with modelled SAR peak locations? *Phys Med Biol*. 2010;56:439.
63. Kok HP, Ciampa S, Kroon-Oldenhof R, et al.. Toward online adaptive hyperthermia treatment planning: correlation between measured and simulated specific absorption rate changes caused by phase steering in patients. *Int J Radiat Oncol Biol Phys*. 2014;90:438-445.
64. Kok HP, Straten L, Bakker A, et al.. Online adaptive hyperthermia treatment planning during locoregional heating to suppress treatment-limiting hot spots. *Int J Radiat Oncol Biol Phys*. 2017;99:1039-1047.
65. Zanoli M, Trefná HD. Combining target coverage and hot-spot suppression into one cost function: the hot-to-cold spot quotient. In: *2021 15th European Conference on Antennas and Propagation (EuCAP)*. IEEE; 2021:1-4.
66. Wust P, Rau B, Gellermann J, et al. Radiochemotherapy and hyperthermia in the treatment of rectal cancer. In: Delaini GG, ed. *Rectal Cancer*. Springer; 1998:175-191.
67. Oleson JR, Samulski TV, Leopold KA, et al.. Sensitivity of hyperthermia trial outcomes to temperature and time: implications for thermal goals of treatment. *Int J Radiat Oncol Biol Phys*. 1993;25:289-297.
68. Aklan B, Zilles B, Paprottka P, et al.. Regional deep hyperthermia: Quantitative evaluation of predicted and direct measured temperature distributions in patients with high-risk extremity soft-tissue sarcoma. *Int J Hyperthermia*. 2019;36:169-184.
69. Kok HP, Schooneveldt G, Bakker A, et al.. Predictive value of simulated SAR and temperature for changes in measured temperature after phase-amplitude steering during locoregional hyperthermia treatments. *Int J Hyperthermia*. 2018;35:330-339.

How to cite this article: Zanoli M, Trefná HD. Suitability of eigenvalue beam-forming for discrete multi-frequency hyperthermia treatment planning. *Med. Phys.* 2021;1–17. https://doi.org/10.1002/mp.15220